Fluorescence Imaging Study of Impinging Underexpanded Jets

Jennifer A.(Wilkes) Inman[*], Paul M. Danehy[†], Robert J. Nowak[‡], and David W. Alderfer[§]
NASA Langley Research Center, Hampton VA, 23681-2199

An experiment was designed to create a simplified simulation of the flow through a hole in the surface of a hypersonic aerospace vehicle and the subsequent impingement of the flow on internal structures. In addition to planar laser-induced fluorescence (PLIF) flow visualization, pressure measurements were recorded on the surface of an impingement target. The PLIF images themselves provide quantitative spatial information about structure of the impinging jets. The images also help in the interpretation of impingement surface pressure profiles by highlighting the flow structures corresponding to distinctive features of these pressure profiles. The shape of the pressure distribution along the impingement surface was found to be double-peaked in cases with a sufficiently high jet-exit-to-ambient pressure ratio so as to have a Mach disk, as well as in cases where a flow feature called a recirculation bubble formed at the impingement surface. The formation of a recirculation bubble was in turn found to depend very sensitively upon the jet-exit-to-ambient pressure ratio. The pressure measured at the surface was typically less than half the nozzle plenum pressure at low jet pressure ratios and decreased with increasing jet pressure ratios. Angled impingement cases showed that impingement at a 60° angle resulted in up to a factor of three increase in maximum pressure at the plate compared to normal incidence.

Nomenclature

D_e	=	nozzle exit diameter
D_{imp}	=	impingement distance, measured from nozzle exit plane to impingement target
JPR	=	jet pressure ratio (ratio of nozzle exit to ambient pressure)
NO	=	nitric oxide
p_0	=	nozzle plenum pressure
p_a	=	test chamber (ambient) pressure
p_e	=	static pressure at nozzle exit
p_{max}	=	maximum (peak) pressure
PLIF	=	planar laser-induced fluorescence
Re_{exit}	=	Reynolds number at nozzle exit
RTF	=	Return to Flight
V_e	=	velocity at nozzle exit
μ_e	=	dynamic viscosity at nozzle exit
θ_{imp}	=	impingement angle
ρ_e	=	density at nozzle exit

I. Introduction

In the wake of the loss of the Columbia orbiter due to a breach in the leading edge of its left wing, a series of tests were conducted in an effort to better understand the flowfields resulting from breaches in the outer structure of reentry vehicles. Penetration of hot gas through breaches could impact internal structures, causing failure of the

[*] Research Scientist, Advanced Sensing and Optical Measurement Branch, MS 493, AIAA Member
[†] Research Scientist, Advanced Sensing and Optical Measurement Branch, MS 493, AIAA Associate Fellow
[‡] Research Scientist, Aerothermodynamics Branch, MS 408A, AIAA Member
[§] Research Scientist, Advanced Sensing and Optical Measurement Branch, MS 493

vehicle. These tests were conducted in support of the Orbiter Aerothermodynamics Working Group as part of NASA's Shuttle Return to Flight (RTF) effort. A subset of these tests used planar laser-induced fluorescence (PLIF) of nitric oxide (NO) to visualize the flow issuing from a nozzle into a low-pressure chamber. The flow environments encountered in these tests include regions of low static pressure, turbulent and/or three-dimensional flow structures, and regions of interest with both strong and weak density gradients. Such conditions, though frequently encountered in aerospace simulation facilities, cannot be satisfactorily visualized using traditional path-averaged techniques such as schlieren and shadowgraph, which rely on sufficiently strong density gradients. An alternative approach was therefore required in order to satisfy the objectives of these tests to characterize the features of these nozzle flows. PLIF is a flow visualization technique that provides non-intrusive measurements with sub-millimeter spatial resolution and flow-stopping (1 μs) temporal resolution in many of these challenging testing regimes[1]. PLIF images reveal the size and location of flow structures. Additionally, these images can be used to identify the laminar or turbulent state of these flows[2]. We have previously reported the use of PLIF to investigate free (non-impinging) underexpanded sonic jets[3] and have compared a subset of these results with computational fluid dynamics (CFD)[4]. This paper will focus on the results of the test cases in which the nozzle flow was directed onto the surface of a flat plate (hereafter referred to as the "impingement target") at various distances and angles. A future paper will report the results of these tests in regards to the effect of jet impingement upon the process of transition to turbulence. This paper will mainly focus upon the test cases involving steady, laminar, impinging jet flows.

A major difference between this work and the majority of previous investigations of similar impinging flows by others is that this work focused on relatively low Reynolds numbers, spanning from many fully laminar test cases to transitional and turbulent cases. By contrast, other investigations have generally involved higher Reynolds numbers—up to three orders of magnitude higher than the very highest Reynolds numbers investigated in the present work and well within the turbulent flow regime. Table 1 gives a summary of test conditions for several past investigations.

	M_e	Re_{exit}	JPR (p_o/p_a)	p_a *(atm)*	D_{imp}/D_e	θ_{imp} *(deg)*	Type(s) of measurements
Alvi & Iyer [5] (1999)	1	1.9E6	2.6	1	1.6-2	90	PIV, shadowgraph, acoustic, surface pressure
Donaldson & Snedeker [6,7] (1971)	0.57,1	1.9E5-1.3E6	1-3.57	1	1.96-39.1	15-90	Pitot & surface pressure, grease streak, heat transfer
Kim et al.[8] (2003)	1	9.7E5-2.7E6	1.1-3.7	1	1.6-2	90	Computational (3D unsteady NS)
Lamont & Hunt [9] (1980)	2.2	4.0E6-6.7E6	1.2,2	1	0.75-15	30-90	Shadowgraph, surface pressure
Love & Lee[10] (1958)	1-3	1.7E5-5.7E7	0.25-19, 60-41,820	1, 5e-5	NA	NA	Schlieren, method of characteristics calculations
Stitt [11] (1961)	1-9.85	3.7E4-2.7E7	545-1.5E5	4.7E-4	0.4-40	90	Schlieren, surface pressure, surface erosion
Present work	1, 2.6	170-3.6E4	1-37	1.3E-3 -0.094	10.5-39.5	90, 60, 45	PLIF, surface pressure

Table 1. Comparison of previous underexpanded jet studies with the present investigation. The quantities compared here are, from left to right: nozzle exit Mach number, exit Reynolds number, jet (nozzle-exit-to-ambient) pressure ratio, ambient pressure of test section, impingement distance in nozzle diameters, impingement angle, and type of study and/or measurements.

Another distinction is that these previous studies have generally been concerned with near-field impingement, on the order of a few jet diameters. The impinging jet configurations in the present work, with the closest impingement distance being about 10.5 nozzle diameters and the furthest being 39.5 nozzle diameters, are all relatively far-field compared to the studies listed in Table 1 (with the exception of Stitt.[11] Note also that, even though the investigations of Donaldson and Snedeker[6,7] had some limited data at about 40 nozzle diameters, the vast majority of their data were within about 15 nozzle diameters). In rocket plume/ground interaction applications, ground erosion was a primary concern, and the near field was thus of greatest significance. Many of these studies were conducted at atmospheric pressure. Of the studies listed in Table 1, only those of Stitt[11] and Love and Lee [10] investigated flows into sub-atmospheric pressure environments. For those studies, the intended application was rocket and thruster operation in the vacuum of space, and so the ambient pressures used were one to two orders of magnitude lower than those of the present study, the conditions of which were designed to be relevant to the reentry conditions experienced by the space shuttle orbiter.

In addition to flow visualization, pressure measurements were recorded on the surface of the impingement target. The observed pressure profiles along the centerline of the target were found to fall into two broad categories: those with the maximum pressure corresponding to the centerline of the jet axis, and those with the maximum pressure occurring in an annular ring, away from this axis. PLIF images helped to elucidate the characteristics of the resulting pressure profiles by highlighting the flow structures corresponding to distinctive features of these pressure profiles.

II. Experimental Description

A. Facility and Hardware

Tests were conducted at the NASA Langley Research Center using the test section of the 15-Inch Mach 6 Air Tunnel as a vacuum chamber. For a detailed description of the facility and hardware, see Ref. 12. A schematic of the layout is shown in Fig. 1. Nitrogen or helium seeded with 0.5% nitric oxide was plumbed into a heated stainless steel plenum, through a nozzle, and into the vacuum chamber.

Two different nozzles were used. The geometry of these nozzles is illustrated in Fig. 2. The first was a converging nozzle with a nominal exit Mach number of 1,. This nozzle is hereafter referred to as the *sonic* nozzle. The second was a converging/diverging nozzle with a nominal exit Mach number of 2.6, hereafter called the *supersonic* nozzle. Mass flow controllers controlled the flow rates, which indirectly controlled the plenum pressure upstream of the nozzle.

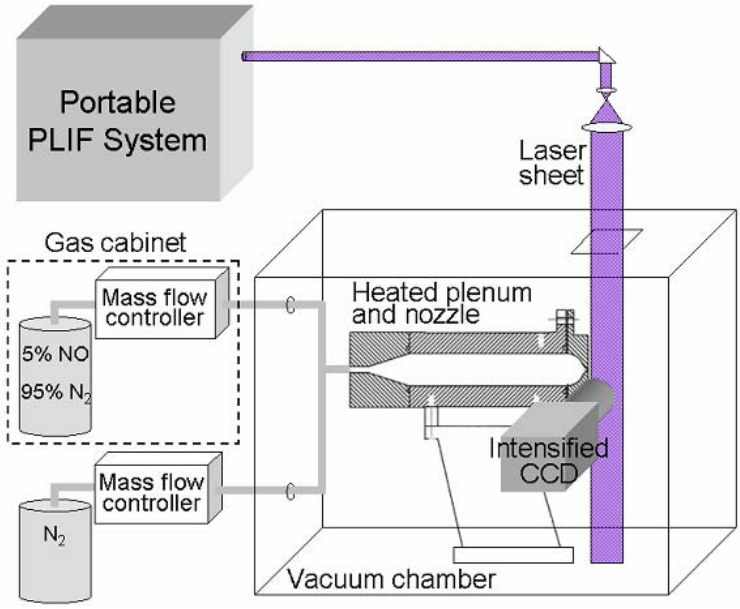

Figure 1. PLIF system and experimental hardware. Gas is plumbed through a heated plenum and nozzle into a vacuum chamber. A laser sheet enters the top of the vacuum chamber and excites nitric oxide molecules in the flow. An intensified CCD camera positioned at right angles to the laser sheet images the fluorescence.

Optics directed a 100mm wide by ~0.2mm (FWHM) thick laser sheet vertically downward through a window in the top of the test chamber. The laser sheet was oriented in a plane perpendicular to the nozzle exit plane. The sheet forming optics were mounted to a translation stage. A stepper motor attached to the translation stage allowed fine adjustment of the spanwise position of the laser sheet.

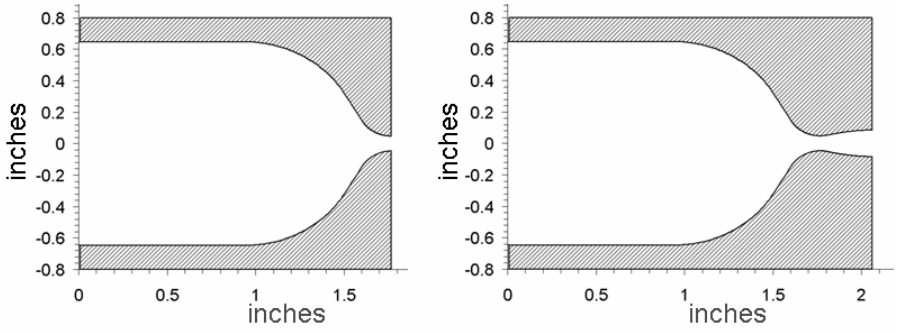

Figure 2. Sonic and supersonic nozzle geometries. The design exit Mach numbers for these two nozzles are 1 and 2.6, respectively.

A 4-inch diameter stainless steel impingement disk was positioned at various distances and angles downstream of the nozzle exit. Figure 3 shows a diagram of this apparatus. The center of this disk included 32 pressure taps. They were spaced 0.045 inches apart, and had an inside diameter of .021 inches. The taps were oriented in a vertical plane (the plane of the laser sheet), on the jet centerline. From the camera's viewing angle, the jet flow was from left to right.

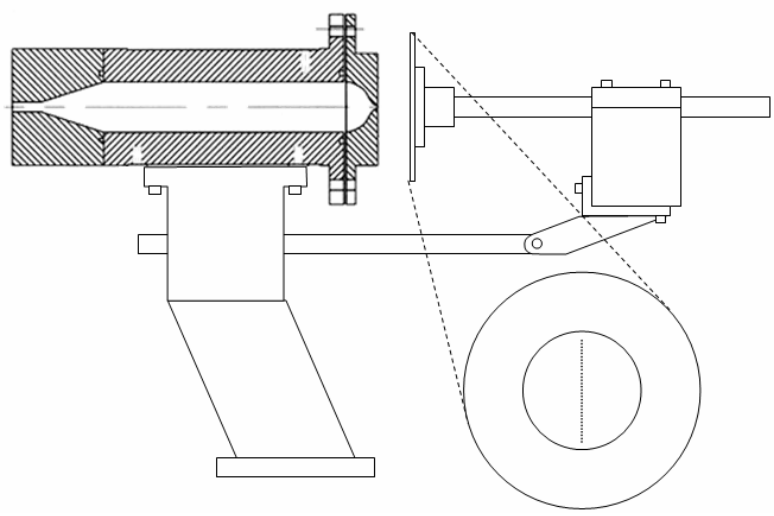

Figure 3. Stainless steel plenum and impingement target hardware. The impingement angle and distance were continuously variable. A close-up view shows the orientation of the 32 pressure taps in the center of the impingement disk.

B. Model Configuration Parameters

Impingement distance was continuously variable from 0 to 6 inches and impingement angle was continuously variable from 90° to 0°, though the minimum impingement distance at non-normal impingement angles was limited by the physical size of the target. In practice, changing impingement distance or angle required approximately a half day of down time, and so a limited number of discrete distances and angles were included in the test matrix. For the majority of cases, the impingement disk was oriented normal to the jet axis (which is defined to be a 90° impingement angle). Two configurations included oblique impingement angles of 45° and 60°. For these cases, the target was rotated clockwise, as viewed from the camera viewing angle, about the horizontal axis perpendicular to the jet axis.

For each hardware configuration, two flow parameters were varied: the exit Reynolds number (Re_{exit}) and the jet pressure ratio (*JPR*). Re_{exit} was defined in terms of the nozzle exit diameter, D_e, and the density ρ_e, velocity V_e, and dynamic viscosity μ_e at the nozzle exit, as given by (1).

$$\mathrm{Re}_{exit} = \frac{\rho_e V_e D_e}{\mu_e} \tag{1}$$

Re_{exit} was varied by changing the mass flow rates and nozzle plenum temperature. *JPR* was defined as the ratio of the static pressure at the nozzle exit, p_e, to the ambient pressure in the test chamber, p_a, according to (2), and was varied by changing the test section pressure for a given Reynolds number (and therefore, a fixed p_e).

$$JPR = \frac{p_e}{p_a} \tag{2}$$

C. Planar Laser-Induced Fluorescence (PLIF) Flow Visualization Technique

The PLIF laser system includes a tunable Nd:YAG-pumped dye laser followed by doubling and mixing crystals. The resulting output, at 226.256 nm, was tuned to excite the strongly fluorescing spectral lines of NO near the Q_1 branch head (Q denotes a change in rotational quantum number equal to zero). Optics formed the beam into a laser sheet that was 100 mm wide x ~0.2 mm thick (FWHM) in the measurement region. Fluorescence was imaged onto a gated, intensified CCD at a viewing angle normal to the laser sheet. Images were acquired at 10 Hz with a 1μs camera gate and a spatial resolution of between 3 and 7 pixels/mm, depending on the required field of view for a given hardware configuration. This system is detailed in Refs. 3, 4, and 12. The PLIF system is also capable of pressure-sensitive and velocity-sensitive flow imaging.

III. Analysis Methods: Flow Visualization Image Processing

Sets of 100 single-shot images were acquired for a range of unit Re_{exit} (177 to 35,700) and *JPR* (1.8 to 38). So-called *background images* were also acquired on each day of testing for a range of vacuum chamber pressures. During the acquisition of these background images, the laser was fired but no gas was flowing through the nozzle. Any nonzero intensity in these background images is attributed to either camera dark current or the laser scatter and room light not blocked by the filter in front of the camera lens. Averaged background images were created from the average of 100 single-shot images in order to smooth out random shot-to-shot variations in background intensity.

Single-shot images were processed to correct for background scattered light and camera dark current as well as mean spatial variations in laser sheet intensity. Conveniently, jet gas containing nitric oxide diffused relatively uniformly into the test chamber in regions away from the jet, but still imaged by the camera. The fluorescence from

the diffuse nitric oxide in these regions provided a convenient laser-energy reference, allowing the spatial variation in the laser intensity to be corrected. This was accomplished on a shot-by-shot basis by first selecting an area of the image above the core of the jet flow and then establishing the average pixel intensity along each column in that region.

Raw images were 512 x 512 pixels; images presented in this paper have been cropped top and bottom to show the regions of greatest interest. In some of the earlier runs, the spatial resolution was determined by imaging a ruler in the same plane as the laser sheet. This process was improved midway through this set of tests, after Run 200. A *dotcard* was used in place of a ruler. Dotcards consisted of a rigid metal plates covered with a sheet of paper. The paper was white with black squares printed in a regular grid pattern. Spatial resolution was calculated by capturing images of a dotcard positioned in the same plane as the laser sheet. The optical access in these experiments permitted perpendicular viewing of the measurement plane and no significant perspective or lens distortion was found in the images.

IV. Results

Table 2 shows the range of conditions and hardware configurations for which data were taken during the impinging jet study. Reynolds numbers and jet pressure ratios were calculated based on nozzle exit conditions. The table list the number of cases that were studied for each combination of hardware configuration and type of PLIF imaging that was investigated in these tests. For each flow visualization case, 100 single-shot images were acquired. The laser sheet was also swept spanwise through the flow, providing slices of the flow field, though these results are not shown here. The velocity-sensitive, pressure-sensitive, and density-sensitive imaging data are not presented in this paper, with the exception of one pressure-sensitive image in Fig. 9.

	Supersonic Nozzle				Sonic Nozzle		
Impingement configuration	*FV / VI*	*V*	*P*	ρ	*FV / VI*	*V*	*P*
1" @ 90°					25		5
1.75" @ 90°	25	22	22	1	25		
2.5" @ 90°	22	19	21		24		
2.5" @ 60°	18						
3.75" @ 90°	23				23		
3.7" @ 45°	23						
5" @ 90°	22						
∞ (free jet)	88	11		12	53	8	8
Re_{exit}	600-14,000				2,400-35,000		
JPR	1-16				3-27		

Table 2. Matrix of configurations for which data were acquired in the impinging jet cases. *FV/VI* indicates *flow-visualization* and *volume-imaging* runs, *V* indicates *velocity* runs, *P* indicates *pressure-sensitive* runs, and ρ indicates *density-sensitive* runs.

A. Characteristic Flow Structures

1. Sonic and supersonic free jet structures

Free (non-impinging) laminar jet cases are seen to exhibit flow structures that are similar to those of other cases having the same *JPR*[12]. That is, two laminar cases with similar *JPR*s but different Reynolds numbers will appear more similar than two cases with the same Reynolds numbers but different *JPR*s. For sonic nozzle cases, flows can be divided into two major groups: those with a repeating diamond shock structure, and those with a barrel shock structure, a Mach disk, and a streamwise high-velocity jet boundary (seen for flows with *JPR*s greater than about 3).[2,3] The diamond shock structure is seen for *JPR*s less than about three, such as in Fig. 4, where several diamond shock cells can be seen in the first several jet diameters downstream of the nozzle exit. Figures 5 and 6 show higher JPR PLIF images resulting in an underexpanded jet issuing from a sonic nozzle. Key flow structures are labeled in these figures. Figure 5 shows the nozzle plenum, nozzle exit, and ambient conditions, as well as the major shock structures and relative Mach numbers in each region of the flow. Additional flow features are labeled in Fig. 6. The arrows within the high-velocity jet boundary qualitatively indicate the velocity profile of the gas in this region. For a good description of the flow features shown in these figures, see Refs. 5 and 12.

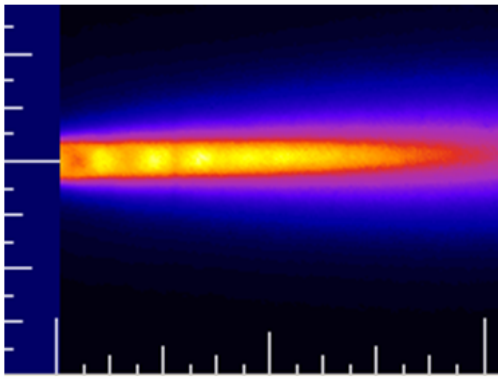

Figure 4. Diamond shock pattern in flow from sonic nozzle. This image is a 100-shot average of a flow with *JPR* = 1.9 and Re_{exit} = 417 (Run 5). The scales are in inches, with the smallest hash marks measuring 1/16th in.

For cases with the Mach 2.6 supersonic nozzle, the division between repeating shock patterns and barrel shock/Mach disk patterns happens at a *JPR* of about 4. For smaller *JPR*s, a repeating pattern analogous to the diamond shock pattern is evident, with a chain-like pattern of alternating spatial minima (high-pressure nodes) and maxima (low-pressure antinodes). This oscillating flow pattern can be seen for two cases in Fig. 7. As *JPR* increases, the wavelength of this oscillating pattern decreases. As a result, the number of cell structures within a fixed distance decreases for larger *JPR*s. Above a *JPR* of about 4, high pressure nodes are no longer evident, and as *JPR* continues to increase, the oscillations in the high-velocity jet boundary gradually decrease. Even larger *JPR*s lead to a modified barrel shock structure—elongated into a more egg-like shape than its comparable sonic jet counterpart—with a Mach disk and a streamwise high-velocity jet boundary, as shown in Fig. 8. In the upper image, note how the upper and lower jet boundaries appear parallel to one another. The lower image was acquired with greater magnification, and the shock and expansion reflections in the high-velocity jet boundary (labeled in Fig. 6) are visible in this lower image.

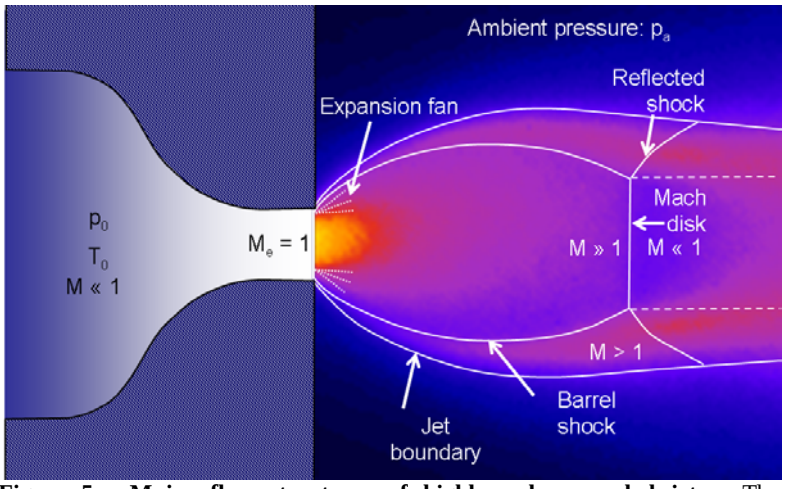

Figure 5. Major flow structures of highly-underexpanded jets. The appearance of a Mach disk is associated with jet pressure ratios greater than about 3 for the sonic nozzle and greater than about 4 for the supersonic nozzle.

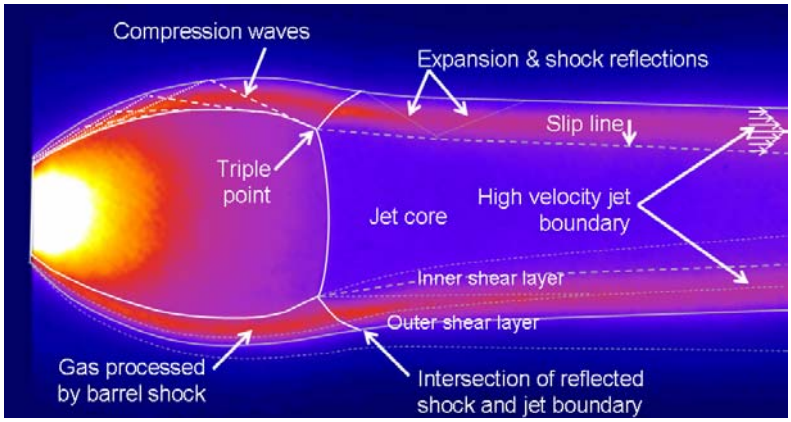

Figure 6: Detailed flow structures of highly-underexpanded sonic jets. PLIF image is from Run 56 with *JPR* = 29.1 and Re_{exit} = 4,294.

2. Impinging jet structures

Impinging jet flows can be divided roughly into three regions: the jet flow upstream of the impingement region, the impingement region, and the wall jet flow (where the flow has become parallel to the surface of the impingement target). For steady flows, the flow structures that are observed in the upstream region are essentially identical to those in free jet cases. Impingement region flow structures are described below. In the wall jet region, several factors act to decrease the intensity of the fluorescence. First, mixing of the jet fluid with the ambient gas is enhanced by the physical dispersion of the jet gas. This results in a decreasing mole fraction of nitric oxide as the gas moves away from the jet centerline. This, in turn, results in a reduction of fluorescence signal near the plate, and so the details of the flow in the wall jet region are not necessarily well-resolved.

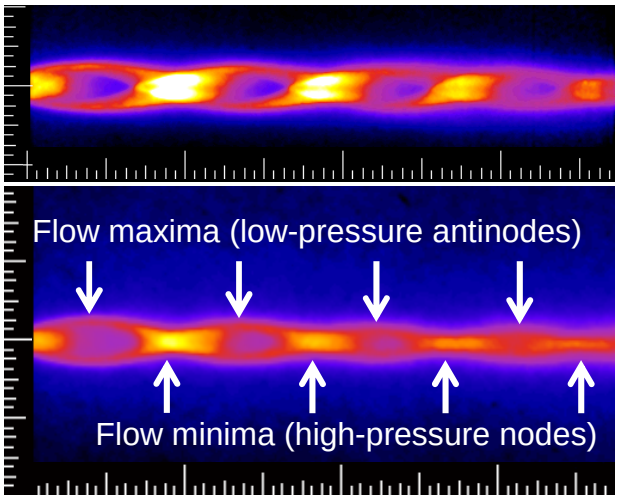

Figure 7. Underexpanded supersonic jets at low pressure ratios. Images are 100-shot averages Top: Run 354, *JPR* = 2.0, Re_{exit} = 4,605; bottom: Run 222, *JPR* = 3.0, Re_{exit} = 3,370, Arrows mark examples of flow minima and maxima. Scales are in inches; the smallest hash marks measure 1/16th in.

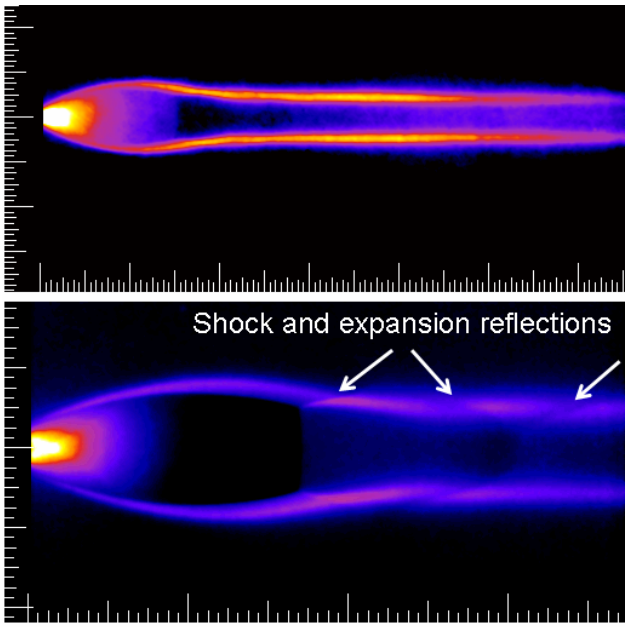

Figure 8. Supersonic free jets with Mach disks and parallel high-velocity jet boundaries. Both images are 100-shot averages. The first image is from Run 236, with *JPR* = 16.2 and Re_{exit} = 13,104; the second is from Run 347 with *JPR* = 12.6 and Re_{exit} = 10,173. Scales are in inches; the smallest hash marks measure 1/16th in. Note the magnified scale of the lower image.

Flows in the impingement region may exhibit several additional flow structures. When the flow impinging on the flat plate is supersonic, a normal shock parallel to the impingement surface, called a *plate shock*, may be formed.[5] Under certain flow conditions, a high pressure bubble of gas may build up between this shock and the impingement surface, causing the shock to move further away from the surface.[13,14] Choosing to excite pressure-sensitive spectral lines[12] at a laser wavelength of 225.693 nm (in which the fluorescence signal is most strongly dependent on pressure, with much weaker dependence on temperature) makes identification of such a *stagnation bubble* (also called a *recirculation bubble*) and/or normal plate shock much easier, as the pressure rise inside the recirculation region results in a large increase in intensity compared to the free jet region. Figure 9 illustrates this, with two images of similar flows, taken with the laser at two different frequencies. Both images are averages of 100 single-shots of supersonic flows, taken at an impingement distance of 1.75 in. (10.7 nozzle diameters). The image on the left was acquired with the laser tuned to flow visualization lines (226.256 nm). The image on the right was taken with the laser tuned to pressure-sensitive lines (225.693 nm). Note the well-defined boundaries of the recirculation bubble in the pressure-sensitive image as compared with the flow-visualization image. By contrast, note the lack of signal in the low pressure region inside the barrel shock in the pressure-sensitive as compared to the flow-visualization image, where there is signal throughout the flow and the jet boundary is more clearly defined.

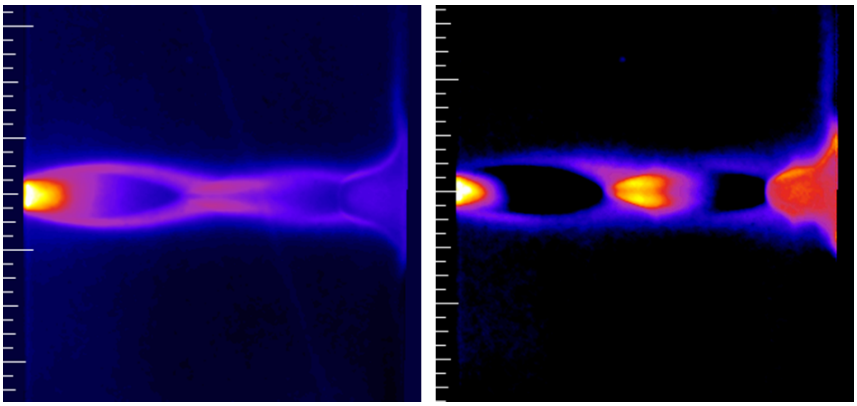

Figure 9. Comparison of flow visualization and pressure-sensitive PLIF. Left: *JPR*=3.1 (Run 363). Right: *JPR*=3.0 (Run 451). D_{imp}/D_e=10.7 (1.75 in.) for both. The scales are in inches, with the smallest hash marks measuring 1/16th in.

Several studies in the literature have discussed the formation of recirculation bubbles for some combinations of jet pressure ratio and impingement distance. Alvi et al.[15,5] give a good description of recirculation bubble formation. Mackie and Taghavi[16] found that recirculation bubble formation was purely a three-dimensional phenomena; that is, two dimensional jets (quasi-two dimensional in experimental studies, or truly two-dimensional in computational studies) never resulted in recirculation bubble formation. This is less surprising in the experimental cases (which can never be truly two-dimensional), since the recirculation bubble is shaped like a bell, and requires the annular pressure "seal" around the ring where it intersects with the impingement plate in order to be a stable feature. The gas inside the recirculation bubble acts as a high-pressure reservoir, contained by the plate shock upstream, the high-velocity jet boundary impingement along the outer edge, and the impingement disk surface.

B. Flow Structure Comparison with Pressure Profiles

Consider an impinging jet flow with a uniform momentum profile throughout the core of the jet. One would expect the pressure profile of such a jet to resemble a top hat function, with roughly uniform pressure across the intersection of the jet with the impingement target, dropping to near ambient pressure away from the core of the jet. Modifying the situation to include viscous effects, one would expect to see a decrease in momentum—and therefore a decrease in pressure on the impingement surface—along the edges of the jet. This modified pressure profile would be peaked in the center, smoothly dropping off to the ambient pressure toward the edges of the jet flow. In fact, for some cases, this describes the pressure profiles that have been measured. An example is shown in Fig. 10. The PLIF image on the left and the graph of measured impingement pressure on the right are shown aligned and equally scaled, so that the vertical axis on the graph matches the vertical location along the impingement plate in the image. All pressure profiles presented herein are time-averaged.

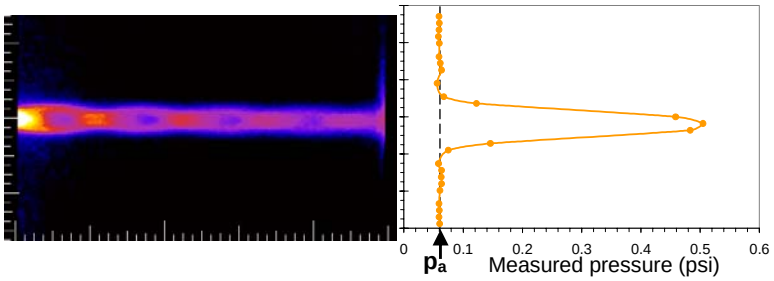

Figure 10. Pressure profile with a single, central peak. This profile is for supersonic nozzle Run 544 with *JPR* = 1.5, Re_{exit}= 1,317, θ_{imp}= 90° and D_{imp}/D_e= 15.2, p_a=0.062 psi. A dashed line indicates the ambient pressure. A single-shot PLIF image from this run is shown on the left. The scales on both the image and the graph are in inches, with the smallest hash marks equal to 1/16th in.

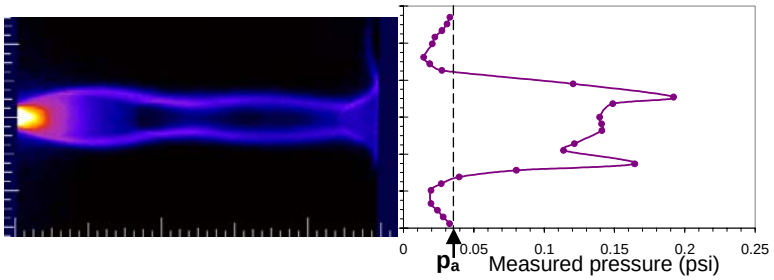

Figure 11. Pressure profile with a double peak. This profile is for supersonic nozzle Run 536 with *JPR* = 5.4, Re_{exit}= 2,302, θ_{imp}= 90° and D_{imp}/D_e= 15.2, p_a=0.035 psi. A dashed line indicates the ambient pressure. A single-shot PLIF image from this run is shown on the left. The scale on the image is in inches, with the smallest hash marks equal to 1/16th in.

For some flow conditions, the pressure profiles are quite different than the smooth single-peaked profile predicted by the simple explanation. For example, some profiles typically exhibit a double-peaked structure, with the maximum pressure occurring away from the flow centerline. The peaks in pressure are found to coincide with the location of the impingement of the high-velocity jet boundary or with the intersection of the shock structure surrounding a recirculation bubble. Fluid mechanically, this can be understood because the high-velocity jet boundary carries with it a great deal of the momentum and thus creates a larger pressure rise as it impinges on the flat plate, compared to the slower jet core, which has passed through a normal shock wave at the Mach disk. The pressure between these peaks is often nearly constant, while the pressure outside these peaks drops off toward—and sometimes dips briefly below—the ambient pressure. Figure 11 shows an example of this type of profile. The high-velocity jet boundary impinges on the flat plate, and is partly reflected. That is, the flow does not immediately become tangent with the wall, but rather first appears to reflect off the surface before becoming a pure wall jet. This results in an annular suction region beneath the place where the flow is skipping above the surface, where the pressure is actually *lower* than ambient. Figure 12 shows a close up of the flow in Fig. 11. This is a case with a strong suction ring. Arrows identify the regions of maximum and minimum pressure,

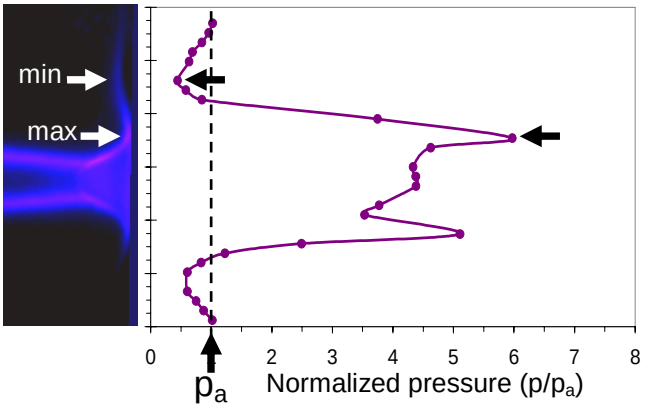

Figure 12. Relation of flow features to the maximum and minimum measured pressures. The PLIF image is a close-up of the impingement region for the flow in Fig. 11 and is show to scale with the graph. The smallest hash marks on the vertical scale of the graph are 1/16th in.

clearly illustrating the connection between flow features and surface pressures. A dashed vertical line indicates the ambient pressure (the pressure has been normalized by this pressure). Note that the actual peak pressures may occur between pressure taps, and thus may be greater than the measured peak pressure.

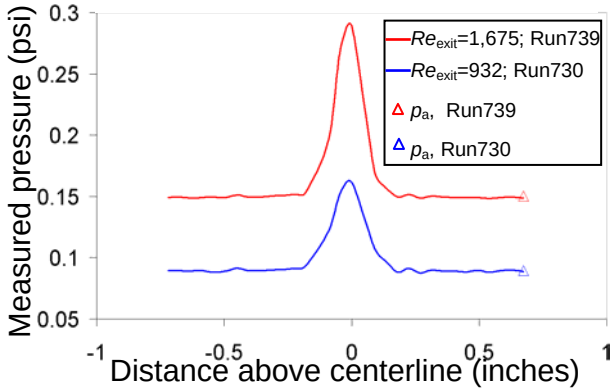

Figure 13. Measured pressure profiles. Two impingement surface pressure profiles from laminar runs with the same jet pressure ratio but different exit Reynolds numbers are shown.

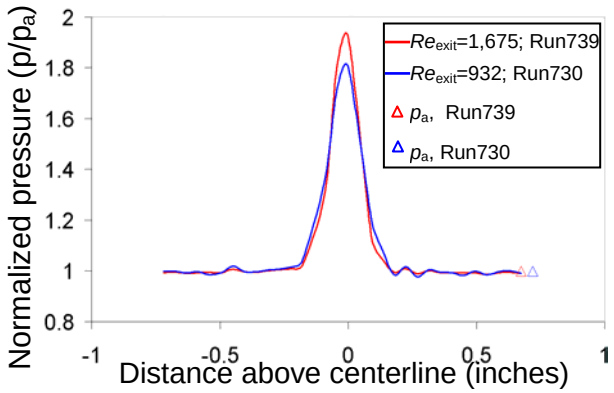

Figure 14. Normalized pressure profiles. This shows the same impingement surface pressure data as Fig. 13, normalized by the ambient (chamber) pressure of each run. This normalization results in nearly self-similar profiles.

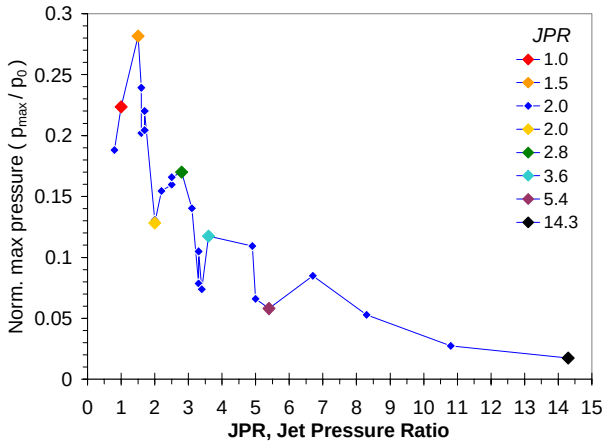

Figure 15. Supersonic nozzle recovery pressure as a function of JPR for one impingement distance, 90° impingement. D_{imp} / D_e =15.2 (2.5 in.). Data from runs having exit Reynolds numbers ranging from 380 to 12,500 are included in this graph.

C. Reynolds Number Effect on Pressure Profiles

Like their free jet counterparts, the shape of impinging jet flow structures are similar for those runs that have similar *JPR*s (for a given nozzle type), so long as the runs are all laminar. It is then not surprising that the shapes of the pressure distributions for runs with the same *JPR* have similar features. However, for runs with matching *JPR* but different values of Re_{exit}, the magnitude of the measured pressure profiles increases with increasing Re_{exit}. This is expected to be the case because, for constant gas plenum temperatures, Re_{exit} is proportional to plenum pressure (p_0). Self-similar pressure profiles can be obtained for runs with the same *JPR* by normalizing all the measured impingement disk pressures by either p_0 or p_a.

Figures 13 and 14 graphically depict the effect of normalization by p_a. Figure 13 shows pressure profiles from two runs with essentially the same *JPR* (2.8), but different values of Re_{exit} (1,675 and 932). Figure 15 shows these same data after they have been normalized by the ambient pressure for either run. The two normalized profiles exhibit a high degree of overlap.

D. Jet Pressure Ratio Effect on Pressure Profiles

The shape of the pressure profile was found to depend heavily on the jet pressure ratio. To illustrate this, consider Figs. 15-17. In Fig. 15, the maximum (peak) pressure (p_{max}) has been graphed versus *JPR*. Data have been included for both steady and unsteady laminar supersonic runs with an impingement distance (D_{imp}) of 15.2 nozzle diameters (2.5 in.) and impingement angle θ_{imp} of 90°. In this graph, the pressures have been normalized by the nozzle plenum pressure (p_0). Peak pressures are significant in aerothermal applications because they may be associated with regions of peak heating. The maximum pressure, normalized by the plenum pressure, will be called the *recovery pressure* to indicate that this quantity represents the maximum plate pressure as a fraction of the stagnation pressure. Keep in mind that the discrete (as opposed to continuous) nature of the pressure taps results in measured peak pressures that are less than or equal to the actual peak pressure, which may occur between taps.

In Fig. 15, notice that the recovery pressure for this nozzle/plate configuration is always less than 0.3. Next, notice that for *JPR*s of less than about 5, the values are seen to exhibit relatively large variations around the apparent mean. Above about 5, the value of the recovery pressure is seen to decline smoothly,

without these large fluctuations. The oscillations that are seen for low *JPR*s are not simply noise in the data, but corresponds to variations in flow structures that are very sensitive to small changes in *JPR* in this region. The colored data points in Fig. 15 correspond to the PLIF images and their associated pressure profiles shown in Fig. 16. The images are labeled by their *JPR*. The number of cells (that is, the number of low-pressure antinodes or flow maxima) between the nozzle exit and the impingement target is seen to decrease for increasingly large *JPR*, from about 4 cells in the second image, to about 2 ½ cells in the fifth image. In the sixth image, no high-pressure nodes are evident. Instead, this image and the last image both show a flow with a barrel shock and normal Mach disk.

As a further illustration of the dependence of the recovery pressure on *JPR*, consider Fig. 17. Here, pressure profiles are shown for two runs with very similar jet pressure ratios. The top profile has a double-peaked structure, whereas the bottom profile is single-peaked. This is due to the existence of a recirculation bubble in the top image, and the lack of such a feature in the bottom image. The sudden emergence or disappearance of a recirculation bubble that results for small changes in *JPR* is an effect known as *staging*.[12] Staging behavior is the exhibition of non-continuous phenomena in a flow, or rather, discrete jumps from one continuous region (or *stage*) to another. This staging behavior causes the oscillations shown in Fig. 15. Subsequent peaks of these oscillations correspond to different numbers of nodes, and also correspond to swapping between single and double peaked pressure profiles.

For supersonic normal impingement cases with *JPR*s above about 4, a double-peaked pressure profile was always seen, even in cases with no recirculation bubble. In such cases, the peak pressures were found to occur at the intersection of the high-velocity jet boundary with the impingement target.

The behavior of the recovery pressure as a function of *JPR* is shown in Fig. 18 for four supersonic normal impingement (θ_{imp}=90°) configurations with different impingement distances. All four configurations are similar to that shown in Fig. 15 in that they all show fluctuations in peak pressure for *JPR*s associated with oscillating flow structures and show a lack of fluctuations for higher *JPR*s associated with flows having a Mach disk. Interestingly, the behavior appears to be relatively independent of impingement distance, at least for the range of impingement distances (10.7-30.5 nozzle diameters) in this study. A solid black line denotes a

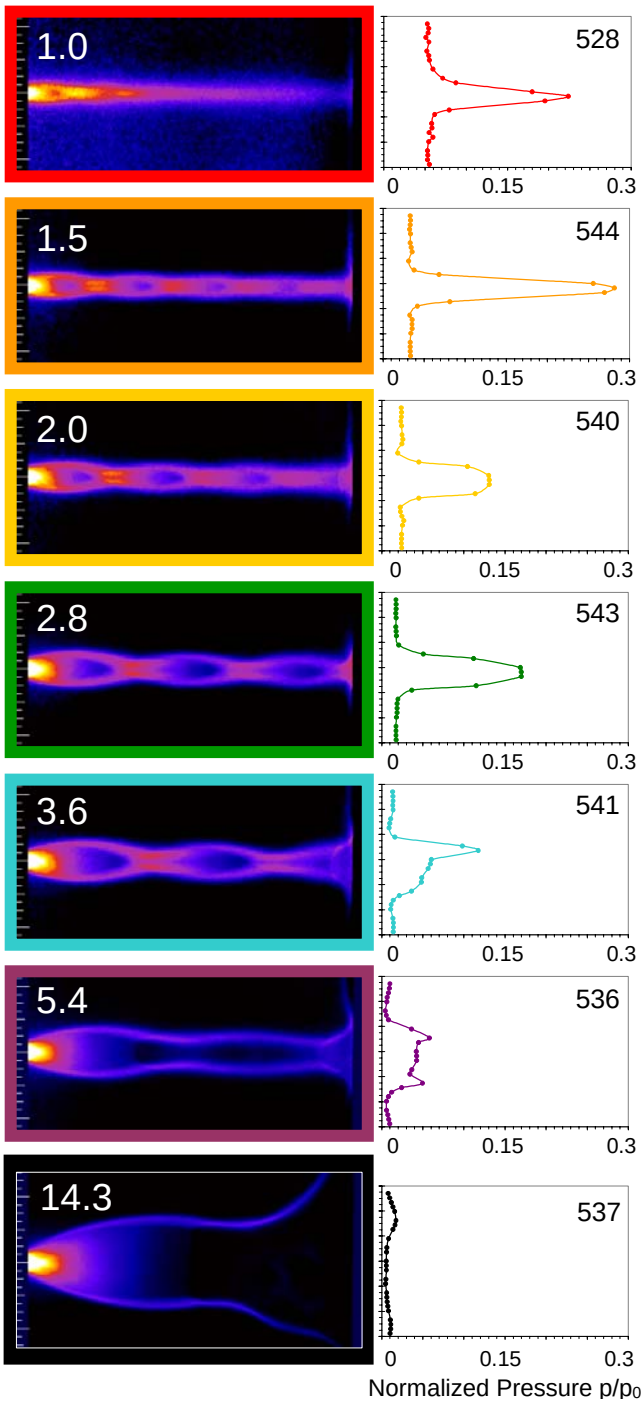

Figure 16. Single-shot PLIF images and the corresponding normalized pressure profiles for the colored data points in Fig. 15. *JPR* are listed in white on each figure and run numbers are listed in black in the upper right-hand corner on each graph. All runs have θ_{imp}=90°, D_{imp} /D_e = 15.2 (2.5 in.). The smallest hash marks on the scales are 1/16th in.

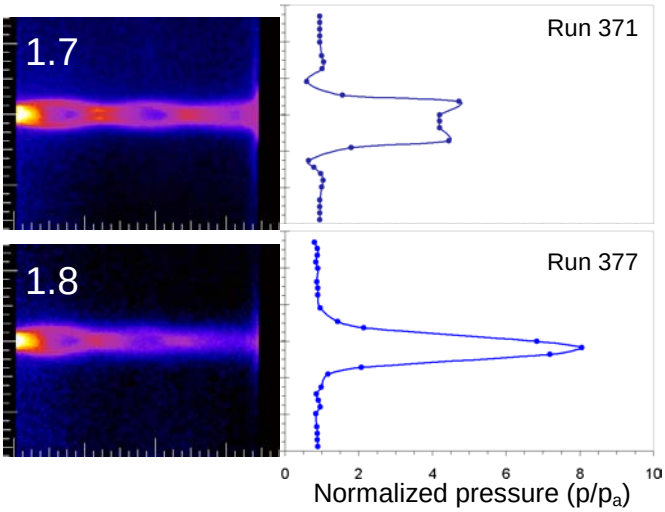

Figure 17. Staging effect in impingement pressure profiles. Graphs show the sensitivity of profile features to small changes in *JPR*, for two cases with θ_{imp}= 90° and D_{imp} / D_e = 10.7 (1.75 in.). The upper image is for *JPR* = 1.7 (Run 371) and the lower images is for *JPR* = 1.8 (Run 377). Pressures have been normalized by the ambient pressure, p_a. Scales on images and vertical scales on graphs are in inches, with smallest hash marks equal to 1/16th in.

proposed empirical model for the mean behavior of the recovery pressure (neglecting the higher order oscillations around the mean). The equation for the empirical model is given by Eq. (3):

$$\frac{p_{max}}{p_0} = \frac{0.34}{JPR} \qquad (3)$$

This coefficient in Eq. (3) was found by performing a least squares fit to the data for *JPR* > 1.5. Note particularly that, for impingement distances between about 10 and 30 nozzle diameters, this result does not depend on impingement distance. This relation may not hold for arbitrarily large or small impingement distances, so caution is warranted in its application to flows outside the range of tested configurations. But within this range, one can see that the recovery pressure for supersonic (Mach 2.6) underexpanded (*JPR* >1.5) jets, the recovery pressure will be less than 0.34 times the plenum pressure. The decrease in recovery pressure at large jet pressure ratios results partially from the increased surface area over which the jet flow impacts the impingement target. An additional effect may result from the pressure losses associated with normal shock waves (the Mach disk) at higher *JPR* versus the oblique shocks associated with oscillating flow structures at lower *JPR*.

Although Fig. 18 indicates that the *peak* pressure is found to be somewhat independent of distance for supersonic nozzle cases, the shape of the pressure profile does change with distance. This is illustrated in Fig. 19. Four single-shot PLIF images are shown for four runs with similar *JPR* but different impingement distances. Pressure profiles (normalized by p_0) are shown on the same graph. Note that the pressure transducer at the -0.135 in. location was faulty and so it appears that the peak pressure was not captured on both sides of the jet for two of the cases. The pressure profiles are all double-peaked (as expected since these flows all have Mach disks and *JPR* > 5) and all have similar peak pressures. However, the pressure deficit near the jet centerline is more or less pronounced, depending on distance. One explanation for this is that the intersection of the jet with the impingement target sometimes occurs near a high-pressure node (flow minima), but other times occurs at a lower-pressure antinode (flow maxima). When the intersection occurs at a node, the pressure difference between the core and outer high-velocity boundary of the jet is less than when the intersection occurs at an antinode. A secondary effect may result from the loss in total pressure associated with the Mach disk. Immediately downstream of the Mach disk, the centerline gas is subsonic (see Fig. 5). Further downstream, viscous effects exert their influence through the inner shear layer (see Fig. 6), and the centerline velocity begins to recover. Likewise, the impingement pressure is

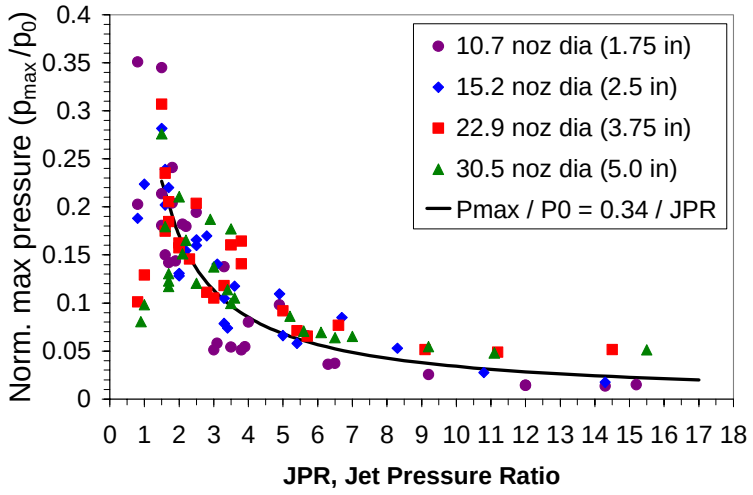

Figure 18. Supersonic nozzle recovery pressures for four impingement distances, 90° impingement. The black line shows a plot of Eq. (3).

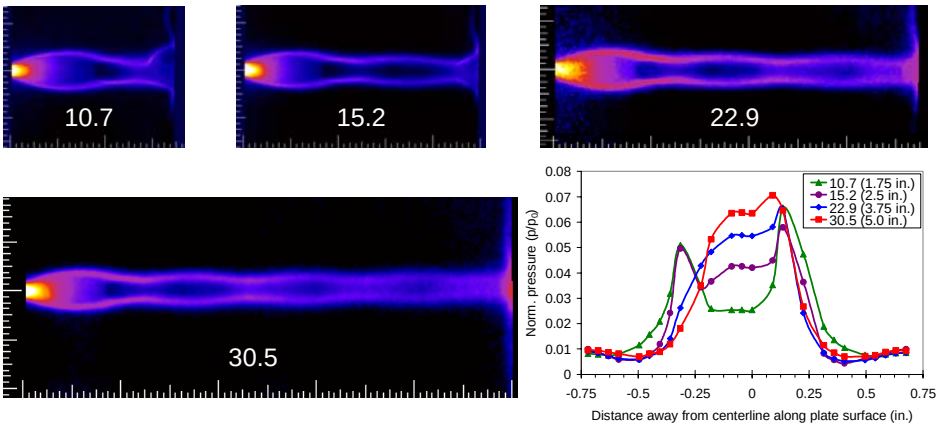

Figure 19. Similar supersonic jet conditions (*JPR* ~5.7) at four impingement distances. Single-shot images are labeled according to the corresponding value of D_{imp}/D_e (nozzle diameters). In order of increasing distance, they are 1.75 in. (Run364), 2.5 in. (Run553), 3.75 in. (Run578), and 5.0 in. (Run605). Note that the peak pressure in the 3rd and 4th cases probably occurred near the location of a faulty pressure transducer at -0.135 in.

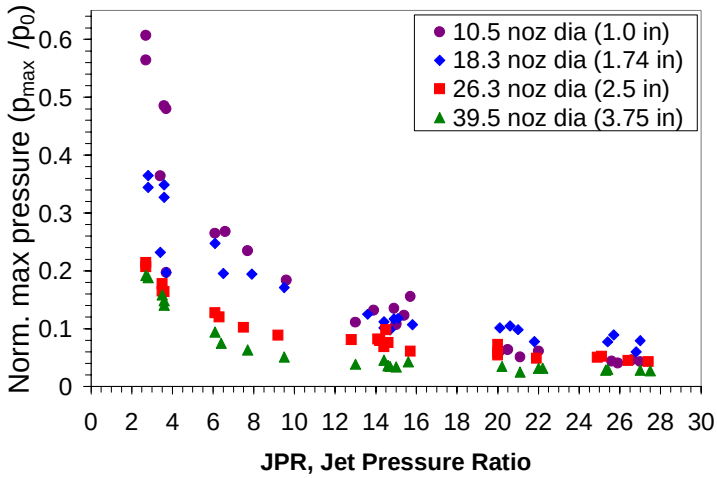

Figure 20. Sonic nozzle recovery pressures, 90° impingement. Smaller impingement distances are seen to result in larger recovery pressures, especially for small *JPR*. No data were taken at *JPR* less than about 2.5, so the maximum possible recovery pressure was not determined. For small impingement distances and low *JPR*, it may approach the plenum pressure.

reduced along the centerline immediately downstream of the Mach disk, but may gradually recover as the impingement distance is increased.

For sonic nozzle cases, slightly different trends are observed. Figure 20 shows recovery pressure as a function of *JPR* for four different impingement distances. Like the supersonic nozzle cases, peak pressures are observed to decrease with increasing *JPR*. Additionally, oscillations are again observed for the region of low *JPR* (less than about 3), the same flow regime in which oscillating flow structures are manifest. However, oscillations are not observed for the two larger impingement distances (26.3 and 39.5 nozzle diameters). It has been previously noted that the spatial wavelengths associated with sonic nozzle flows tended to be smaller than their supersonic nozzle counterparts (on the order of 2 nozzle diameters in length, versus 3 to 8 nozzle diameters in length in the case of a supersonic nozzle), and that diamond shock structures in low *JPR* sonic nozzle flows tended to dampen out after 2 or 3 oscillations[12]. So at larger impingement distances, flow oscillations are no longer present (see Fig. 4, for example), and so do not result in staging behavior of impingement pressure. The sonic cases also exhibit an inverse relationship of recovery pressure to *JPR*. However, unlike the supersonic cases, the sonic cases show a dependence on impingement distance, with larger recovery pressures associated with smaller impingement distances, especially for low *JPR*s. For these sonic impingement cases, no simple empirical model passes through all the data.

E. Angled Impingement

In the literature, some studies (most notably, the experimental studies of Lamont and Hunt[9], as well as the computational studies of Wu et al.[17] which simulated flows at conditions identical to those of Lamont and Hunt) found that the maximum impingement pressure on angled impingement targets could be much greater (up to a factor of three greater) than the maximum pressure in the corresponding normal impingement cases. In our experiments, we have observed results consistent with these observations. Figure 21 shows three single shot images from runs at three impingement angles and their associated normalized pressure profiles. Although 45° and 60° configurations were not tested at the same impingement distances, the results shown in Fig. 18 and described above suggest that a rough comparison might still be made among runs at different impingement distances.

As previously stated, measured peak pressures may be less than actual peak pressures, due to the finite nature of the pressure measurements performed, and compounded by several faulty pressure transducers. Nevertheless, of the recorded pressures, the graph in Fig. 21 shows that the normalized peak pressure in the 60° case is roughly twice that of the 45° case and roughly three times that of the 90° case, in agreement with prior experimental[9] and computational[17] studies. By closely examining the images associated with these runs, it is seen that in the 60° configuration, the high-velocity jet boundary along the bottom of the jet impacts the impingement target at nearly normal incidence, which likely results in a pressure maximum at that point. By contrast, at 45°, this part of the flow strikes the plate at a slightly more glancing angle. In both cases, the upper boundary of the jet impacts the target at a gentler angle, resulting in asymmetric pressure profiles with peak pressures below the jet centerline. Figure 22 shows the recovery pressure plotted as a function of *JPR* for all 45° and 60° supersonic impingement cases. The general trend is for increased recovery pressure for 60° cases relative to 45° cases for low values of *JPR*.

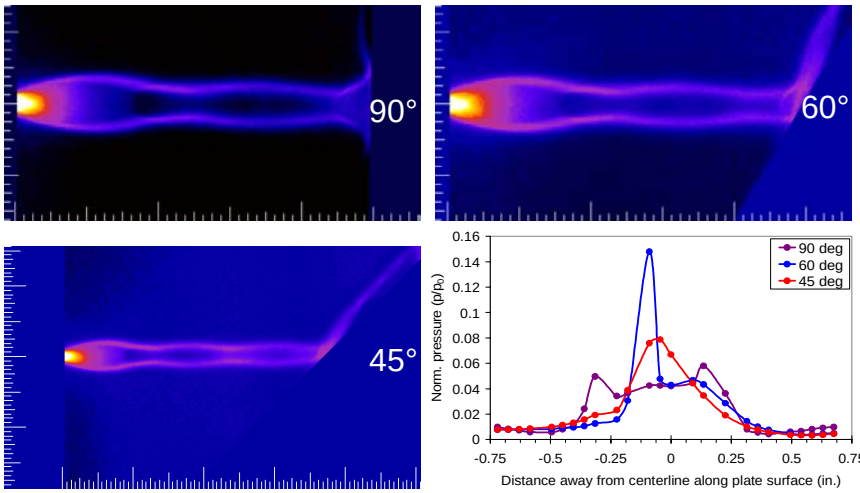

Figure 21. Three impingement angles. Single shot images are shown for similar jet conditions (supersonic nozzle, *JPR* ~5.7, Re_{exit} ~2,300), and θ_{imp}=90° (Run536), 60° (Run553), and 45° (Run630). For the first two, D_{imp}/D_e= 15 (2.5 in); for the third, D_{imp}/D_e= 23 (3.7 in). Note that the peak pressure in the 45° case probably occurred near the location of a faulty pressure transducer at -0.135 in.

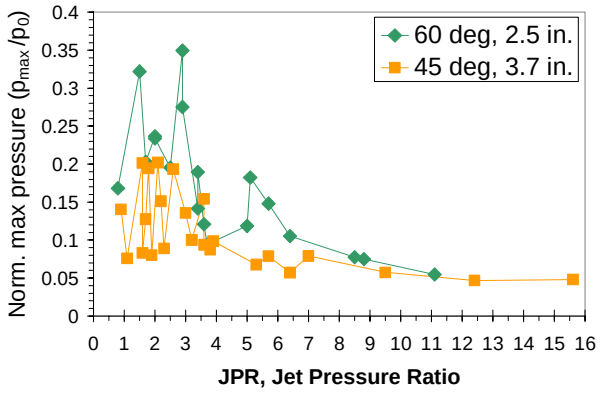

Figure 22. Supersonic nozzle recovery pressures for 45° vs. 60° impingement. Somewhat higher peak pressures are seen in the 60° cases.

V. Conclusion

PLIF images have been used to visualize free and impinging underexpanded jet flows and have provided detailed information about flow structures. The insights into flow structure characteristics provided by PLIF images have helped to elucidate the results of pressure measurements taken at the surface of a flat impingement target and have shed light on the features of the pressure distributions across the face of the target. Under certain conditions, the shape of these pressure distributions was seen to be a very sensitive function of jet pressure ratio; under other conditions, the dependence was rather insensitive to *JPR*. In all cases, the absolute magnitude of the measured pressures was seen to be a linear function of plenum pressure, and therefore, of Reynolds number. The recovery pressure (that is, the peak pressure relative to the plenum pressure) was found to oscillate for low *JPR* and then decrease as the inverse of the jet pressure ratio for high *JPR*. In supersonic nozzle cases, this trend was found to be relatively independent of impingement distance for the cases studied. In sonic nozzle cases, it was found to depend inversely on impingement distance as well. Finally, it was found that recovery pressure was greater for angled impingement than for normal impingement with 60° impingement angle having three times higher peak pressure than normal incidence. These results, while providing good test cases for computations, demonstrate the significant contribution that flow visualization can provide in the understanding and interpretation of surface measurements.

Acknowledgments

The authors wish to acknowledge the collaborative input of Scott Halloran of Rocketdyne, Don Picetti of The Boeing Company and Chris Glass of NASA Langley Research Center, as well as the technical assistance of David Alderfer, Stephen Jones, and Paul Tucker, also of NASA Langley Research Center. They also wish to acknowledge the image processing work done by Aiyana Garcia, a graduate physics student from The College of William and Mary and a NASA GSRP (Graduate Student Researchers Program) student. This work was funded as part of the Shuttle Return to Flight effort through Chuck Campbell of Johnson Space Center and Tom Horvath of NASA Langley Research Center. Support was also received from the Aeronautics Research Mission Directorate's Fundamental Aeronautics Hypersonic Project, Experimental Capabilities discipline, under Robert Okojie.

References

[1] J. L. Palmer and R. K. Hanson, "Shock tunnel flow visualization using planar laser-induced fluorescence imaging of NO and OH," *Shock Waves*, vol. 4, pp. 313-323, 1995

[2] J. A. Inman, P. M. Danehy, R. J. Nowak, and D.W. Alderfer, "Identification of Instability Modes of Transition in Underexpanded Jets," *38th AIAA Fluid Dynamics Conference, Seattle, WA, 23-26 June 2008* (to be published).

[3] J. A. Wilkes, P. M. Danehy, and R. J. Nowak "Fluorescence Imaging Study of Transition in Underexpanded Jets," *Proceedings of the 21st International Congress on Instrumentation in Aerospace Simulation Facilities (ICIASF)* [CD-ROM], Sendai, Japan, 29 August – 1 September 2005, pp. 1-8.

[4] J. A. Wilkes, C. E. Glass, P. M. Danehy, and R. J. Nowak, "Fluorescence Imaging of Underexpanded Jets and Comparison with CFD," *44th AIAA Aerospace Sciences Meeting and Exhibit*, AIAA-2006-0910, Reno, NV, 9-12 January 2006.

[5] Alvi, F.S. and K.G. Iyer, "Mean and Unsteady Flowfield Properties of Supersonic Impinging Jets with Lift Plates," *5th AIAA/CEAS Aeroacoustics Conference*, AIAA 99-1829, Bellevue (Greater Seattle), WA, 10-12 May 1999.

[6] Donaldson, C. D., and R. S. Snedeker, "A study of free jet impingement. Part 1. Mean properties of free and impinging jets," *J. Fluid Mech.* **45**, 1971, Part 2: 281-319.

[7] Donaldson, C. D., R. S. Snedeker, and D. P. Margolis, "A study of free jet impingement. Part 2. Free jet turbulent structure and impingement heat transfer," *J. Fluid Mech.* **45**, 1971, Part 3: 477-512.

[8] Kim, Sung In, and Seung O. Park, "Unsteady Flow Simulation of Supersonic Impinging Jet," *41st AIAA Aerospace Sciences Meeting and Exhibit*, AIAA 2003-621, Reno, NV, 6-9 Jan 2003.

[9] Lamont, P.J., and B.L. Hunt, "The Impingement of Underexpanded Axisymmetric Jets on Perpendicular and Inclined Flat Plates," *Journal of Fluid Mechanics* **100**: 471-511, 1980.

[10] Love, E. S. and L. P. Lee, "Shape of Initial Portion of Boundary of Supersonic Axisymmetric Free Jets at Large Pressure Ratios," NACA TN 4195, January 1958.

[11] Stitt, Leonard E., "Interaction of Highly Underexpanded Jets with Simulated Lunar Surfaces," Lewis Research Center, Cleveland, OH. NASA Technical Note D-1095, December 1961.

[12] Inman, Jennifer A., "Fluorescence Imaging Study of Free and Impinging Supersonic Jets: Jet Structure and Turbulent Transition," Ph.D. Dissertation, Department of Physics, The College of William and Mary, Williamsburg, VA, 2007.

[13] Henderson, Brenda, "The connection between sound production and jet structure of the supersonic impinging jet," *Journal of the Acoustical Society of America* **111** (2): 735-747, Feb 2002.

[14] Henderson, B., J. Bridges, and M. Wernet, "An experimental study of the oscillatory flow structure of tone-producing supersonic impinging jets," *Journal of Fluid Mechanics*, Cambridge University Press, **542**: 115-137, 2005.

[15] Alvi, F.S., J.A. Ladd, and W.W. Bower, "Experimental and Computational Investigation of Supersonic Impinging Jets," *AIAA Journal* **40** (4): 599-609, April 2002.

[16] Mackie, S. and R. Taghavi, "Supersonic Impinging Jets: A Computational Investigation," *40th AIAA Aerospace Sciences Meeting and Exhibit*, Reno, NV. AIAA 2002-0671, 14-17 Jan. 2002.

[17] Wu, J., L. Tang, E.A. Luke, X-L. Tong, and P. Cinnella, "A Comprehensive Numerical Study of Jet Flow Impingement over Flat Plates at Varied Angles," *39th AIAA Aerospace Sciences Meeting and Exhibit*, AIAA-2001-0745, Reno, NV, 8-11 Jan 2001.

Extended abstract to be submitted to: 46th AIAA Aerospace Sciences Meeting and Exhibit, Reno, NV, 7-10 January 2008

Fluorescence Imaging Study of Impinging Underexpanded Jets

Jennifer A. (Wilkes) Inman*†, Paul M. Danehy†, Robert J. Nowak†, and David W. Alderfer†

*email address: jennifer.a.inman@nasa.gov
† NASA Langley Research Center, Hampton VA, 23681-2199

I. Introduction

The tests that will be described in this paper were designed to create a simplified simulation of the flow through a hole in the surface of a supersonic aerospace vehicle and the subsequent impingement of the flow on internal structures. They were conducted in support of the Orbiter Aerothermodynamics Working Group as part of NASA's Shuttle Return to Flight (RTF) effort. Planar laser-induced fluorescence (PLIF) of nitric oxide (NO) is used to visualize the flow. PLIF images show the size and location of flow structures, and the laminar or turbulent state of these flows can also be ascertained from these images.

The flow environments encountered in these tests include regions of low static pressure, turbulent and/or three-dimensional flow structures, and regions of interest with both strong and weak density gradients. Such conditions, though frequently encountered in aerospace simulation facilities, cannot be satisfactorily visualized using traditional path-averaged techniques such as schlieren and shadowgraph, which rely on sufficiently high static pressures and strong density gradients. An alternative approach was therefore required. PLIF is a powerful flow visualization technique that provides a means of making non-intrusive measurements with sub-millimeter spatial resolution and flow-stopping temporal resolution in many of these challenging testing regimes [1]. We have previously used PLIF to investigate underexpanded sonic jets [2] and have compared a subset of these results with computational fluid dynamics (CFD) [3].

In addition to flow visualization, pressure measurements were recorded on the surface of an impingement target. PLIF images helped to elucidate the characteristics of the resulting pressure profiles by highlighting the flow structures corresponding to distinctive features of these pressure profiles.

II. Experimental Methods

A. Facility and Hardware

Tests were conducted at NASA Langley Research Center using the test section of the 15-Inch Mach 6 Wind Tunnel as a vacuum chamber. Nitrogen or helium seeded with 0.5% nitric oxide was plumbed into a heated stainless steel plenum, through a nozzle, and into the vacuum chamber. Two different nozzles were used: the first—a converging nozzle with the exit at the smallest diameter, or throat, and hereafter referred to as the "sonic" nozzle—had a nominal exit Mach number of 1; the second—a converging/diverging nozzle, hereafter called the "supersonic" nozzle—had a nominal exit Mach number of 2.6. Mass flow controllers controlled the flow rates, which indirectly controlled the plenum pressure upstream of the nozzle.

A 4-inch impingement disk was positioned at various distances and angles downstream of the nozzle exit. The center of this disk included 32 pressure taps. They were spaced 0.045 inches apart, and had an inside diameter of .021 inches. The taps were oriented in a vertical plane (the plane of the laser sheet), on the jet centerline. From the camera's viewing angle, the jet flow was from left to right.

B. Model Configuration Parameters

For the majority of cases, the impingement disk was oriented normal to the jet axis (which is defined to be a 90° impingement angle). Two configurations included oblique impingement angles of 45° and 60°. (For these cases, the target was rotated clockwise, as viewed from the camera viewing angle, about the horizontal axis perpendicular to the jet axis.) Impingement distance was continuously variable from 0 to 6 inches. In practice, changing impingement distance or angle required approximately a half day of down time.

For each hardware configuration, two flow parameters were varied: the exit Reynolds number (Re_{exit}) and the jet pressure ratio (*JPR*). Re_{exit} was defined in terms of the nozzle exit diameter, D_e, and the density ρ_e, velocity V_e, and

dynamic viscosity μ_e at the nozzle exit, as given by (1).

$$\mathrm{Re}_{exit} = \frac{\rho_e V_e D_e}{\mu_e} \quad (1)$$

Re_{exit} was varied by changing the mass flow rates and nozzle plenum temperature. *JPR* was defined as the ratio of the static pressure at the nozzle exit, p_e, to the ambient pressure in the test section, p_a, according to (2), and was varied by changing the test section pressure for a given Reynolds number (and therefore, a fixed p_e).

$$JPR = \frac{p_e}{p_a} \quad (2)$$

C. PLIF Flow Visualization Technique

The PLIF laser system includes a tunable Nd:YAG-pumped dye laser followed by doubling and mixing crystals. The resulting output, at 226.256 nm, was tuned to excite the strongly fluorescing spectral lines of NO near the Q_1 branch head (Q denotes a change in rotational quantum number equal to zero). Optics formed the beam into a laser sheet that was 100 mm wide x ~0.2 mm thick (FWHM) in the measurement region. Fluorescence was imaged onto a gated, intensified CCD at a viewing angle normal to the laser sheet. Images were acquired at 10 Hz with a 1μs camera gate and a spatial resolution of between 3 and 7 pixels/mm, depending on the required field of view for a given hardware configuration. This system is detailed in Ref. 2 and Ref. 3. The PLIF system is also capable of pressure-sensitive and velocity-sensitive flow imaging. Although data were acquired under these conditions, those results will be reported in a future paper.

	Supersonic Noz.				Sonic Nozzle		
Impingement configuration	*FV / VI*	*V*	*P*	*ρ*	*FV / VI*	*V*	*P*
1" @ 90°					25		5
1.75" @ 90°	25	22	22	1	25		
2.5" @ 90°	22	19	21		24		
2.5" @ 60°	18						
3.75" @ 90°	23				23		
3.7" @ 45°	23						
5" @ 90°	22						
8 (free jet)	88	11		12	53	8	8
Re_{exit}	600-14,000				2,400-35,000		
JPR	1-16				3-27		

Figure 1. Test matrix for impinging jet cases. FV/VI = flow visualization and volume imaging; V = velocity-sensitive imaging; P = pressure-sensitive imaging; ρ = density-sensitive imaging. Because Reynolds numbers and jet pressure ratios were calculated based on nozzle exit conditions, the range of Re and JPR for supersonic nozzle cases is less than for sonic nozzle cases. The controlling limitation was the inability to achieve steady chamber pressures below 1 or 2 Torr (0.2 – 0.4 psi).

III. Experimental Results

Figure 1 shows the range of conditions and hardware configurations for which data were taken during the impinging jet study. Reynolds numbers and jet pressure ratios were calculated based on nozzle exit conditions. The table list the number of cases that were studied for each combination of hardware configuration and type of PLIF imaging that was investigated in these tests. For each flow visualization case, 100 single-shot images were acquired. The laser sheet was also swept spanwise through the flow, providing slices of the flow field, a technique hereafter called "volume imaging." These slices allow us to reconstruct cross-sections of the flow in planes perpendicular to the jet axis, as described in the following section. As previously stated, we plan to report the results of the velocity-sensitive, pressure-sensitive, and density-sensitive imaging data in a future publication, but not in this paper.

A. Characteristic Flow Structures

The data show that free jet cases having the same JPR exhibit the similar flow structures, so long as the cases under consideration are all laminar. For sonic nozzle cases, flows can be divided into two major groups: those with a repeating diamond shock structure (seen for flows with JPRs less than about 3), and those with a barrel shock structure, a Mach disk, and a streamwise high-velocity jet boundary (seen for flows with JPRs greater than about 3)[2]. For cases with the supersonic nozzle, the division happens at a JPR of about 4. For smaller JPRs, a repeating pattern, analogous to the diamond shock pattern, is evident, with a chain-like pattern of alternating spatial minima and maxima. As JPR increases, the repeating pattern becomes less pronounced. Larger JPRs lead to a modified barrel shock structure—elongated into a more egg-like shape than its comparable sonic jet counterpart—with a Mach disk and a streamwise high-velocity jet boundary.

Sometimes these flow structures are more readily understood by using volume imaging data to reconstruct spanwise slices of the flow. The full paper will describe this process in more detail. An example is shown in Figure 2. The top image in the figure shows a single-shot image from the centerline of the flow. The six images in the bottom of the figure are cross-

sectional slices at various axial locations in the flow.

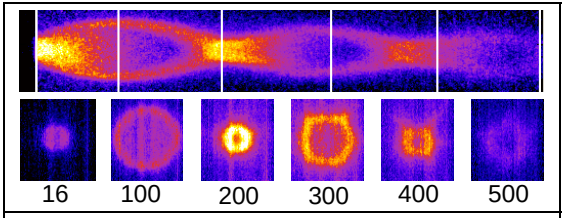

Figure 2. PLIF volume imaging. The white lines on the upper single-shot centerline image show the axial locations for which reconstructed cross-sectional slices are shown. The numbers below the cross-sectional images indicate the column number in the original image, which is 512 columns wide.

B. Flow Structure Relation to Pressure Profiles

Consider an impinging jet flow with a uniform momentum profile throughout the core of the jet. One would expect the pressure profile of such a jet to resemble a top hat function, with roughly uniform pressure across the intersection of the jet with the impingement target, dropping to near ambient pressure away from the core of the jet. Modifying the situation to include viscous effects, one would expect to see a decrease in momentum—and therefore a decrease in pressure on the impingement surface—along the edges of the jet. This modified pressure profile would be peaked in the center, smoothly dropping off to the ambient pressure toward the edges of the jet flow. In fact, for some cases, this describes the pressure profiles that have been measured.

But for other cases, the actual profiles are quite different. Such profiles typically exhibit a double-peaked structure, with the maximum pressure occurring away from the flow centerline. The pressure between these peaks is often nearly constant, while the pressure outside these peaks drops off toward—and sometimes dips briefly below—the ambient pressure. Flow visualization images acquired in the present study have helped to elucidate the origin of these hallmark features by highlighting the flow structures associated with presence of the impingement surface. These images also help to explain the observed sensitivities (and insensitivities) of the pressure profiles to Reynolds number and jet pressure ratio, as explained further in the following two sections.

C. Reynolds Number Effect on Pressure Profiles

Like their free jet counterparts, impinging jet flow structures are similar for those runs that have similar JPRs (for a given nozzle type), so long as the runs are all laminar. It is then not surprising that the shapes of the pressure distributions for runs with the same JPR have similar features. However, for runs with matching JPR but different values of Re_{exit}, the magnitude of the measured pressure profiles increases with increasing Re_{exit}. This is expected to be the case because, for constant gas plenum temperatures, Re_{exit} is proportional to plenum pressure (p_0). Self-similar pressure profiles can be obtained for runs with the same JPR by normalizing all the measured impingement disk pressures by either p_0 or $p_{chamber}$.

Figure 3 graphically depicts the effect of normalization by $p_{chamber}$. The upper image shows pressure profiles from two runs with essentially the same JPR (2.8), but different values of Re_{exit} (4448 and 2476). The lower image shows these same data after they have been normalized by the plenum pressure for each run. The two normalized profiles show a high degree of overlap.

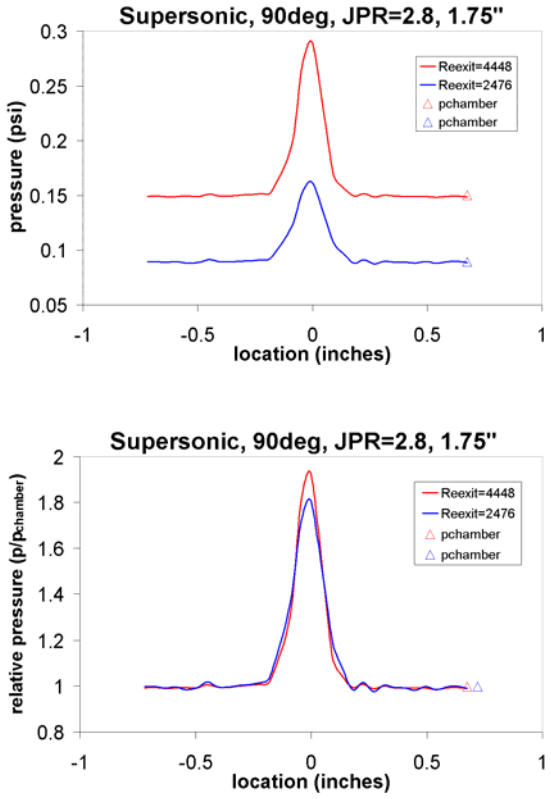

Figure 3. Effect of Reynolds number on pressure profile. Both runs have a jet pressure ratio of 2.8. The red line is for a run with Re_{exit} = 4448; the blue line, Re_{exit} = 2476.

D. Jet Pressure Ratio Effect on Pressure Profiles

The shape of the pressure profile was found to depend heavily on the jet pressure ratio for laminar runs where the impingement target was located in a region of large local spatial variations. That is, JPR small variations in JPR were seen to cause significant variations in the pressure profile for flows where the spatial cross-section is strongly varying with distance in the streamwise direction. This can be explained by considering that small changes in JPR are roughly equivalent to small changes in impingement distance.

For supersonic cases, this sensitivity to JPR was seen for flows with JPRs less than about 4. This effect is illustrated in Figure 4 and Figure 5. Starting in the upper left of Figure 4, PLIF images show the flow structures associated with impinging supersonic axisymmetric jets for increasing JPRs, from about 1.7 to 2.9. In the first image, the jet impinges on the disk just upstream of what would have been the third spatial minimum of the flow (location where the jet diameter is smaller than locations immediately upstream and downstream of that location). As JPR increases in the next three images, the jet then impinges near the third flow maximum, then the second flow minimum, and finally, just downstream of the second flow maximum. Figure 5 shows normalized pressure profiles from these four runs, as well as four additional runs with similar JPRs. As the JPR increases from about 1.7 to about 2.14, the pressure profile becomes narrower and single-peaked (that is, with a single location of the maximum pressure occurring along the centerline of the flow). Then the profiles broaden again, with a marked change around a JPR of about 2.7, including a sudden broadening and the reemergence of a double-peaked structure (with peak pressures occurring along the edges of the jet, and a flattened profile in the subsonic central region of the impingement).

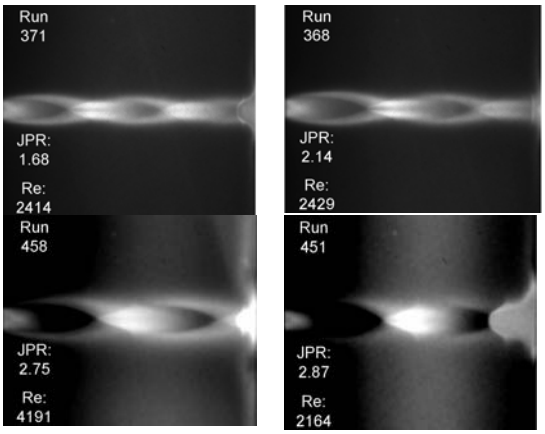

Figure 4 Sensitivity of impingement flow structures to jet pressure ratio (JPR). The chain-like flow structures seen here are reminiscent of the familiar diamond shock pattern seen in sonic jets. Note: the top images are from flow visualization runs; the bottom images are from "pressure" runs, in which the fluorescence intensity is primarily a function of pressure.

Similar sensitivity was not seen for the sonic cases that were studied in these tests. This is likely due to the impingement distances that were chosen. The minimum impingement distance in the sonic nozzle cases was 1.0 inch. Whereas the low JPR supersonic nozzle flows (with JPRs less than about 5) exhibited repeating flow patterns (i.e. spatial frequencies) on the order of 0.5 to 1.25 inches, low JPR sonic nozzle flows had much smaller spatial frequencies—on the order of 0.2 inches. PLIF images show that diamond shock structures tended to dissipate within about 2 or 3 oscillations. Laminar impingement structures for the sonic cases were thus rather indistinct, with little sensitivity to changes in JPR.

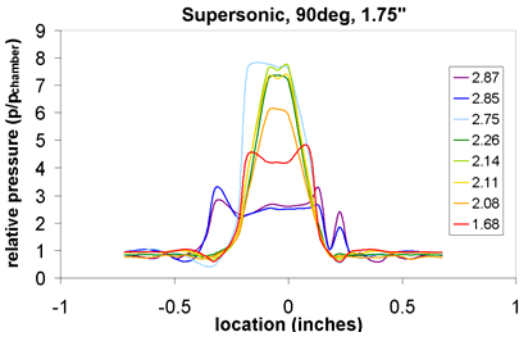

Figure 5 . Pressure profile sensitivity to JPR. These pressure profiles have been normalized by the chamber pressure of the corresponding run.

IV. Conclusions

PLIF images have been used to visualize free and impinging underexpanded jet flows. They have provided detailed information about flow structures and have allowed determination of the laminar, unsteady, or turbulent state of the flow (although the results reported in this paper will be restricted to laminar cases). The insights into flow structure characteristics provided by PLIF images have helped to elucidate the results of pressure measurements taken at the surface of a flat impingement target and have shed light on the features of the pressure distributions across the face of the target. Under certain conditions, the shape of these pressure distributions was seen to be a very sensitive function of jet

pressure ratio; under other conditions, the dependence was rather insensitive to JPR. In all cases, the absolute magnitude of the measured pressures was seen to be a linear function of plenum pressure, and therefore, of Reynolds number. The full paper will include more cases, it will delve into greater detail about the relationship between flow structures and characteristics of pressure profiles (e.g. width, single or double peaks, location of maximum pressure), and it will attempt to place this work in context with the literature on previous studies by others.

ACKNOWLEDGEMENTS

The authors wish to acknowledge the collaborative input of Scott Halloran and Don Picetti of The Boeing Company and Chris Glass of NASA Langley Research Center, as well as the technical assistance of David Alderfer, Stephen Jones, and Paul Tucker, also of NASA Langley Research Center. They also wish to acknowledge the image processing work done by Aiyana Garcia, a graduate physics student from The College of William and Mary and a NASA GSRP (Graduate Student Researchers Program) student. This work was funded as part of the Shuttle Return to Flight effort through Chuck Campbell of Johnson Space Center and Tom Horvath of NASA Langley Research Center.

REFERENCES

[1] J. L. Palmer and R. K. Hanson, "Shock tunnel flow visualization using planar laser-induced fluorescence imaging of NO and OH," *Shock Waves*, vol. 4, pp. 313-323, 1995

[2] J. A. Wilkes, P. M. Danehy, and R. J. Nowak "Fluorescence Imaging Study of Transition in Underexpanded Jets," *Proceedings of the 21st International Congress on Instrumentation in Aerospace Simulation Facilities (ICIASF)* [CD-ROM], Sendai, Japan, 29 August – 1 September 2005, pp. 1-8.

[3] J. A. Wilkes, C. E. Glass, P. M. Danehy, and R. J. Nowak, "Fluorescence Imaging of Underexpanded Jets and Comparison with CFD," *44th AIAA Aerospace Sciences Meeting and Exhibit*, AIAA-2006-0910, Reno, NV, 9-12 January 2006.